Simultaneous Observation of Melt Flow and Motion of Equiaxed Crystals During Solidification Using a Dual Phase Particle Image Velocimetry Technique. Part I: Stage Characterization of Melt Flow and Equiaxed Crystal Motion

ABDELLAH KHARICHA, MIHAELA STEFAN-KHARICHA, ANDREAS LUDWIG, and MENGHUAI WU

A dual phase particle image velocimetry technique is applied to study the flow pattern during a combined equiaxed-columnar solidification process. This technique is able to measure simultaneously the liquid and the equiaxed grain velocity pattern within an academic Ammonium Chloride water ingot. After the formation of a steady convection pattern, solutal buoyancy together with falling crystals destabilize and break the steady convection flow into multiple chaotic cells. In the beginning of the solidification process, the flow transitioned from 2D to a 3D turbulent regime. The kinetic energy for the flow was calculated during the solidification process.

I. INTRODUCTION

MODELING of metallurgical processes is a rapidly expanding field and the research activities in the last decades cover a wide range of areas including melt pretreatment, solidification, and subsequent manufacturing routes. Among those activities, solidification stands in the central position because the primary structure of the materials, and even many defects such as porosity, (macro or micro) segregation, and hot tears, forms during solidification. Those primarily formed structures or defects once existing are difficult to remove or modify by the subsequent material processing.

The more realistic models for describing industry-relevant manufacturing processes, with involvement of solidification, are based on the solution of the macroscopic transport equations (mass, momentum, enthalpy, and species) at the system length scale. Microscopic phenomena such as nucleation, crystal growth kinetics, and thermodynamic equilibria at liquid-solid interfaces are considered with simplified models, which are coupled with the macroscopic transport equations.[1,2]

An important phenomenon in solidification is the simultaneous occurrence of melt flow and crystal motion. Solidification takes place either by a growing columnar front and/or by the growth of equiaxed crystals. Columnar growth happens in the form of cells or dendrites from the mold walls into the bulk melt due to heat extraction from outside. In equiaxed solidification, globular or dendritic crystals form by nucleation or fragmentation and subsequent growth into the surrounding melt. Convection in the melt might have different reasons. Most often, thermal and/or solutal buoyancy together with external body forces occurs. In most of the cases, the flow is unstable and even turbulent. In the case when columnar growth is present, there exists a mushy region where both solid and liquid phases are present. When equiaxed solidification is present, the phases (liquid and equiaxed crystals) interact with each other through momentum and energy exchange. The resulting solid-liquid multiphase flow pattern strongly depends on the microstructure of the equiaxed crystals, which in turn is governed by grain nucleation and growth mechanisms. Because the coupled liquid-solid flow causes structural and chemical inhomogeneities in the final solidified products, a fundamental understanding of the multiphase transport phenomena coupled with the grain nucleation and growth mechanisms is required. The occurrence of dispersed two-phase flows in nature and industrial applications is abundant. The current paper presents some similarity with processes in which dispersed solid particles interact with a carrier flow. However, there is a lack of consistent data to support the numerous theories for flow-particle interaction that have been developed in recent years.[3–8]

In the past, many experimental studies[1–5,9] have been done to investigate the development of the thermo-solutal, also known as double-diffusive, convection during solidification. As a transparent analog for metallic alloys, the NH_4Cl-H_2O solution has proved its convenience to study thermo-solutal convection during columnar solidification. Furthermore, there exist some experimental studies of equiaxed solidification using hypereutectic H_2O-NH_4Cl, mainly presented by Beckermann's group.[10–12] They used the aqueous solution to combine quantitative measurements with visualization of

ABDELLAH KHARICHA, Research Team Leader, MIHAELA STEFAN-KHARICHA, Ph.D. Student, ANDREAS LUDWIG, Professor, and MENGHUAI WU, Associate Professor, are with the Department of Metallurgy University of Leoben, Leoben, Austria. Contact e-mail: abdellah.Kharicha@notes.unileoben.ac.at

two-dimensional equiaxed dendritic solidification. These publications[10–12] proved the powerful means of combined experimental measurements and numerical simulations. In a recent work, Lum et al.[13] successfully applied a laser-based optical method, called molecular tagging velocimetry (MTV), to measure velocity fields in the complex thermo-solutal flows associated with solidification in the presence of significant buoyancy. On the other hand, Beckermann and Wang[10] applied the shadowgraph technique to compare qualitatively the numerically achieved model with experimental results.

Quantitative measurements in differentially heated cavities with solidification were obtained by Wang et al.,[14,15] Ghenai et al.,[16] Skudarnov et al.,[17] and Shih and Tu[18] by means of recent particle image velocimetry (PIV) techniques. Wang et al.[14] employed an advanced PIV technique to measure the velocity field in a cavity subjected to cooling from two vertical walls and the bottom wall. Low concentration solutions were used. Skudarnov et al.[17] and Shih and Tu[18] investigated the effect of the initial solute concentration on the evolution of the convection pattern during solidification. The observed vortexes were described as the result of a double-diffusive convection. In the first stage, the velocity field showed a major circulation loop. Later, many small eddies appeared, and finally several layers of circulation flows were observed. The magnitude of the velocity flow seemed to decrease as solidification proceeded. Almost all pictures presented in the previous works[10,15,18] showed a strong presence of equiaxed crystals not only at the vicinity of the solidification front, but also in the bulk region. Thus, the velocity field obtained from the pictures is based on a mixture of equiaxed crystal and particle seed movements. It is known that equiaxed crystals can develop a relatively large settling or drift velocity.[19,20] The purpose of the present study is to present the results of a new PIV technique that is able to separate the liquid and equiaxed flow.[21–24] This technique is able to measure simultaneously the liquid and the equiaxed velocity magnitude and pattern. It was utilized to measure the complete velocity field during a solidification process in a small cavity cooled from the bottom and two lateral sides.

The PIV technique was introduced elsewhere.[25–28] This technique can measure the whole two-dimensional or three-dimensional flow field simultaneously without disturbing the flow field.[29] To measure the velocity of the fluid, the flow is seeded with small tracer particles with a density similar to the fluid density. A plane of the flow is illuminated by a thin sheet of light. The images of the tracer particles within the plane are recorded twice with a very small time delay of Δt onto a high speed camera. Then, the velocity vectors of the flow are calculated by means of adaptive- or cross correlation of the two subsequent images. The highest peak in the resulting correlation surface indicates the relative displacement for which the best fit between image patterns was obtained and is assumed to represent the real displacement. Errors and limitations that are intrinsic to this technique have been clearly identified by Westerweel.[30]

II. EXPERIMENTAL PROCEDURE

For our quantitative study of the interaction between melt flow and solidification, we have chosen the relatively thin rectangular cavity shown in Figure 1, which was cooled from three sides with a predefined cooling rate. A hypereutectic 29.5 wt pct H_2O-NH_4Cl solution was solidified under controlled conditions. The process was monitored with a two-camera PIV device, whereby a 1-mm-thick cross section in the middle of the test cell was illuminated from the top by Nd-YAG laser pulses.

The cell was made of brass with 1-mm-thick glass plates in the front and at the back. Inside the brass walls, cooling channels which follow a meandering path were designed to achieve a homogeneous temperature. The cooling was controlled by pumping water with a given temperature through the cooling channels.

The H_2O-NH_4Cl solution was prepared by mixing NH_4Cl powder with distillate water and heating to 318.15 K (45 °C) until the powder had completely dissolved. According to the H_2O-NH_4Cl phase diagram, the liquidus temperature of an alloy containing 29.57 wt pct NH_4Cl is 310.15 K (37 °C). Then, fluorescent tracer particles (polyamide particle colored with the Rhodamine B) were added, whereby the solution was intensively stirred. The average diameter of the particles is around 10 μm and their material density is around 1.05 g/cm^3. The density of a 29.5 wt pct NH_4Cl solution at liquidus is about 1.078 g/cm^3 and that of a eutectic NH_4Cl solution is 1.076 g/cm^3. Thus, tracer particles and solution have a similar density (difference 2.7 pct for a 29.5 wt pct NH_4Cl solution and 2.5 pct for the eutectic alloy), and it is reasonable to assume that the particles follow correctly the flow of the solution.

After having added the particles, the solution H_2O-NH_4Cl is poured into the preheated die at 317.15 K (44 °C). This was done slowly in order to prevent capturing of air bubbles. Nevertheless, if air bubbles

Fig. 1—Rectangular cavity used for the controlled solidification experiments. The inner dimensions are $10 \times 10 \times 1$ cm^3.
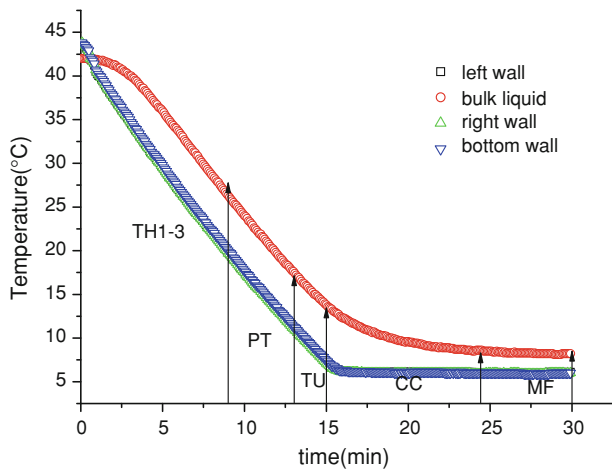
Fig. 2—Evolution of the wall temperatures and the temperature in the upper middle of the liquid solution.

stacked to the cell walls, they were mechanically removed carefully. The filling height was kept at 8 cm. After filling, we waited typically 1 hour to equilibrate the temperature field before we started cooling. In this time, the small, but continuous, heat loss through the front and back window resulted in a steady and symmetric thermal buoyancy flow which was used as the reproducible initial stage for the different experimental runs. Then, the brass cell walls were cooled by 1.2 K (1.2 °C)/min (Figure 2), while the temperature of the brass walls and at the top middle position in the solution was recorded every 5 seconds. In order to avoid condensation of humidity on the glass plates, we stopped cooling when 278.15 K (5 °C) was reached. According to the H_2O-NH_4Cl phase diagram, this corresponds to a solid fraction of 30 pct. Thus, the solidification process terminated with a partly solidified cell.

A. Storage Data and Image Processing Tools

The two-color PIV system adopted in this study comprised a pulsed laser system for illumination, two high speed cameras for image acquisition, a synchronization unit, and a software packet for image and data processing. The laser was a double-pulsed solid-state Nd-YAG and had an output power of 120 mJ with a maximum pulse rate of 21 Hz. The pictures taken by the cameras were in the resolution of 1600×1186 pixels.

Perpendicular to the casting cell, the two CCD cameras were mounted in parallel. The PIV camera mount has a common housing with a shared observation window for the two cameras. This insures straightforward imaging of the same area of the flowing media, while allowing flexible camera positioning. To distinguish the liquid flow from the crystals, a green filter was mounted on one CCD camera (band pass filter of 532 ± 2 nm through which only laser light passes, which was scattered by the equiaxed crystals) and an orange filter on the other camera (high pass filter of 570 ± 2 nm through which only the light passes, which

was reemitted by the fluorescent dye (Rhodamine B)). In this way, the cameras captured images without "interphase" noise, which could then have been processed without any further treatment to obtain the two velocity fields. A set of 20 images was taken every 60 seconds and stored on a PC. The time separating two images was 0.25 seconds which was small enough to catch the time variation of any motion.

Numerous sources of uncertainty exist in such a complex measurement. The positioning of the measurement plane formed by the laser sheet was set as accurate as possible. Nevertheless, an error generated by the laser alignment with respect to the measurement cell of 0.5 pct was unavoidable. The uncertainty related to the PIV technique will be discussed in the next section. The type T thermocouple used had an accuracy of ± 0.1 K (0.1 °C).

B. The Adaptive Correlation and the Particle Tracking Methods

The processing technique used in this study was an adaptive correlation method. Two sequential image maps were subsampled in interrogation areas of 16×16 or 32×32 pixels to obtain the velocity vectors. As usual, the size of the interrogation area depends on the space resolution needed. An overlap of the initial interrogation areas of 50 pct in a horizontal and vertical direction was set. Overlapping of the interrogation areas increases the chance that all particle movements are contained within at least one interrogation area. In numerical practice, the cross correlation of corresponding areas of each image in the image pair is performed, using an FFT-based algorithm, to find the relative displacement that provides the best fit between both particle image patterns. This displacement was taken as the estimation of the mean displacement in the considered area. The theoretic foundations of this technique have been clearly summarized by Westerweel[30] (a more detailed presentation is given in the literature[31]).

An adaptive algorithm for PIV image analyzing may be defined as an algorithm that is able to use the information obtained from the image to further enhance the information recovery and validation process. The aim of the adaptive method is to overcome some of the limitations of the classical standard correlation algorithms.[31,32] Better results were obtained by successively performing the interrogation of the image pair, each time with smaller interrogation areas and using the previously obtained estimation of the displacement field to determine the optimum offset at each location. In this way, the probability that particle images in both frames correspond to the same set of particles does not decay as the size of the interrogation area is reduced. In addition, the signal-to-noise ratio was improved for the correlation obtained with the present method.[31,32]

Correlations are by far the most common approach when dealing with high density seeding images. However, in the present work, the density of equiaxed crystal within an interrogation area could not be guaranteed. When crystal rain occurs, the adaptive correlation technique gives excellent results. However, in areas with

a very low number of equiaxed particles, another method, the particle image tracking, was preferred. The use of this method is valid when the mean distance between particle images is large compared to the particle image diameter or the pixel size. It consists of tracking individual particle images to find the correspondent displacements. The high density limit has been defined by Adrian[25] as the seeding condition for which particle displacements are of the same order of magnitude as the mean spacing between particle images.

C. Validation of the Velocity Vector Field

All the considered interrogation techniques will deliver some small percentage of erroneous velocity vectors. The reasons for the occurrence of these spurious vectors may be found in the limitations of each technique and in the quality of the images. Therefore, special care was given to the recording of the images in order to limit certain amount of noise, owing to ambient light, bad focusing, misalignment, etc. that may deteriorate the signal-to-noise ratio in parts of the image. In addition, a quality control for the obtained vector field as classified by Nogueira et al.[33] was performed in order to discriminate between correct measurements and spurious vectors. The first criterion used to eliminate an unreliable vector is the ratio of the largest to the second largest peak in the cross correlation. If a ratio exceeds the threshold (83 pct) value, then there are two probable values for velocity. In an area with some presence of equiaxed crystals, the second pick in the flow correlation map was clearly identified as the pick corresponding to the equiaxed crystals. The origin of this contamination was due to some diffraction of the light scattered by the tracer particle. Some shadow of crystal can be detected within the flow pictures. For the same reason, it is not possible to follow the flow within the mushy zone. If the second pick was clearly identified as a result of the other phase, the velocity vector was automatically validated even if the threshold for the pick ratio was not reached. For other cases, if a bad result was detected in a single interrogation area, we replaced it by interpolation from the valid neighbors. In case several neighbor interrogations areas did not pass the pick ratio criteria, we chose to delete and not replace the bad vectors. This situation was encountered near the cooling walls where a fast and thin downward jet was present due to the strong thermal buoyancy at the beginning of the experiments.

III. RESULTS

Figure 2 shows the cooling curves of the experiment discussed in the present paper. First, it is obvious that the left, right, and bottom walls reveal the same temperatures. As defined from the circulating coolant, the temperature of the walls dropped by 1.2 K (1.2 °C)/min until the lower temperature limit of 278.15 K (5 °C) was reached. The temperature measured at the top middle position in the solution (labeled in Figure 2 with "bulk liquid") revealed some delay. After about 4 minutes and until 13 minutes, the bulk temperature followed the

same linear variation as the wall temperatures, but at 7 K (7 °C) higher. While the wall temperature reached the lower temperature limit, the difference between wall and bulk liquid temperatures decreased in a Gaussian form.

As mentioned in the previous section, the cell was heated to 317.15 K (44 °C) prior to cooling. Due to a small heat loss via the front and back windows and the constant heating from the brass walls, the temperature measured at the top middle position in the solution cooled down from the pouring temperature of 317.15 K (44 °C) to around 315.15 K (42 °C). Thus, the liquid along the heated brass walls is slightly hotter than in the bulk, and so a typical thermal convection pattern appeared with an upward flow along the vertical walls and a downward flow in the center. This convection pattern was steady and reproducible and canceled any residual motion from pouring. It was thus taken as a well-defined initial condition for the solidification experiments.

As outlined in the following, the process proceeded by passing seven different stages. The first three stages (labeled by TH1, TH2, and TH3) involved only liquid, whereas the last four (labeled by PTH, TU, CC, and MF) involved solidification as well.

A. Thermal Stage 1 (TH1): Initial Thermal Buoyancy

As mentioned before, the experiment started with a steady thermal convection pattern which is shown in Figure 3.

Due to the fact that the temperature measured at the top middle position in the solution turned out to be two degrees below the predefined cell temperature, the liquid in contact with the vertical walls had a tendency to rise by thermal buoyancy. This is at the origin of the symmetric flow pattern shown in Figure 3. The direction of the flow was upward near the vertical walls and downward at the center. As we found that this pattern is
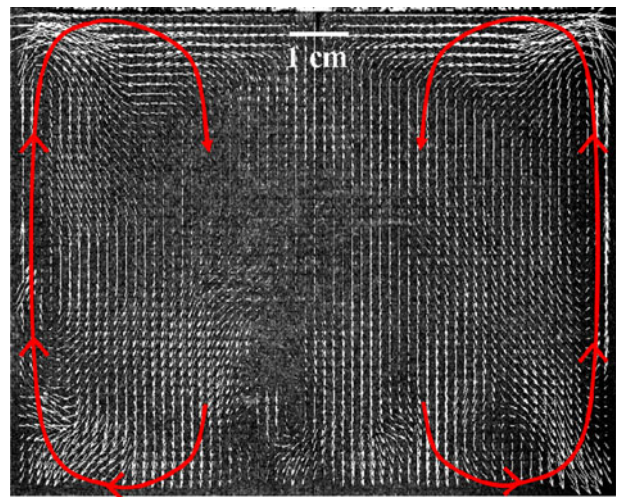
Fig. 3—Melt convection prior to the start of active cooling (thermal stage 1: TH1) measured with PIV. As the slightly hotter walls heated the liquid nearby, it flows upward. The velocity vectors are scaled linearly between $v_{min} = 0.185$ mm/s and $v_{max} = 2.215$ mm/s.
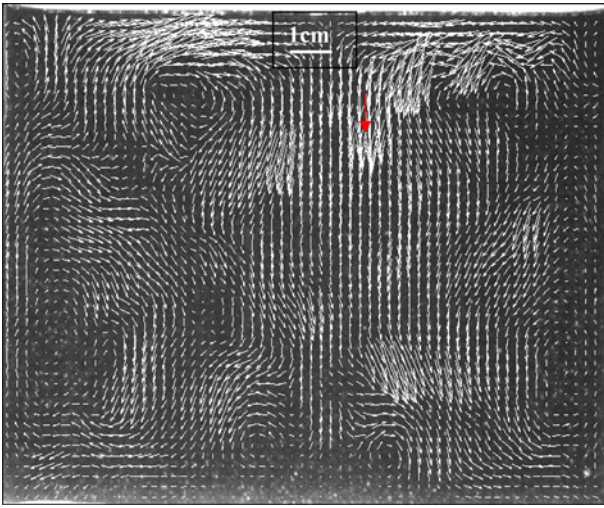
Fig. 4—After the walls' cooling was switched on, the walls' temperature dropped below the temperature of the solution, and thus the upward flow tendency along the vertical walls turned into a downward one. This unstable situation defines the unstable transition stage (thermal stage 2: TH2). The PIV measurement was done $t = 2$ min after the active cooling was started. The velocity vectors are scaled linearly between $v_{min} = 0.03$ mm/s and $v_{max} = 0.37$ mm/s.

Fig. 5—With time, the downward flow near the vertical walls led again to a stable thermal buoyancy pattern (thermal stage 3: TH3). The PIV results shown were taken $t = 8$ min after switching on the cooling. The velocity vectors are linearly scaled between $v_{min} = 0.08$ mm/s and $v_{max} = 1.12$ mm/s.

almost steady, we took it as the initial condition for the experiment.

B. Thermal Stage 2 (TH2): Unstable Transition Stage

We took the moment at which the wall cooling actively started as zero point in time. As now the wall temperature decreases below the temperature of the solution, the former steady convection pattern becomes unstable (Figure 4) and small eddies were emitted from the vertical walls. This stage took typically around 7 to 8 minutes before a new stable flow pattern appeared again.

C. Thermal Stage 3 (TH3): Stable Thermal Buoyancy

When the wall temperature decreases below the temperature of the solution, the liquid close to the vertical walls has a tendency to sink by thermal buoyancy. However, in the experiment, it took 8 minutes until a stable convection pattern established again (Figure 5). This time, the direction of the flow was downward near the walls and upward at the center. As cooling became stronger and stronger, the magnitude of downward flow velocity slightly increased with time. It is clear that the hydrodynamic pattern of this stage was found to be more stable and symmetric than that of stage TH1. Stage TH3 lasted only around 1 to 2 minutes before evidence for solidification appeared. Note that due to the bad correlation, the velocity vectors directly along the vertical walls are not shown in Figure 5.

D. Perturbation of the Thermal State (PTH): Solidification Perturbed Thermal State

Visible solidification, mainly columnar, started at about 9 to 10 minutes after beginning of the cooling. It

did not appear uniformly all over the wall surfaces, but rather in islands of columnar dendritic crystals (Figures 6(a) and (b)). In the vicinity of each columnar island, the flow is immediately disturbed by the presence of one or two small eddies (Figure 6(a)). However, during about the first 3 to 4 minutes of visible solidification, the main pattern of the flow (symmetry, magnitude, main direction) is not changed. Sometimes, the strong downward jet is able to detach columnar structures of up to 5 mm in size from the cooling wall. This phenomenon happens mainly at this stage, rarely in later stages. Few equiaxed crystals were also occasionally observed at the vicinity of the vertical walls (Figure 6(a)). This stage lasted around 3 to 4 minutes.

E. Turbulent Flow State (TU)

As the solidification proceeded, the number of equiaxed crystals increased, and perturbations of the main flow increased in magnitude. A new flow regime with a large number of small eddies appeared (Figures 7(a) and (b)). Now, solidification totally covered the walls and filled about 5 pct of the domain (at the end, ~30 pct is reached). The lake of coherence of the observed eddies, and the presence of strong velocity gradients even far from the walls, is a strong indication of the three-dimensional and turbulent character of this regime. In this stage, large visible equiaxed crystals appeared only near the walls. However, the movement of the small crystals could be evaluated by correlation. This stage lasted around 2 minutes.

F. Coherent Chaotic Flow State (CC)

Out of the turbulent flow stage, a regime where the flow map is coherent, but still chaotic, appeared (Figure 8(a)). The characteristic eddy size was of about 1.5 to 2 cm, and thus larger than the distance between
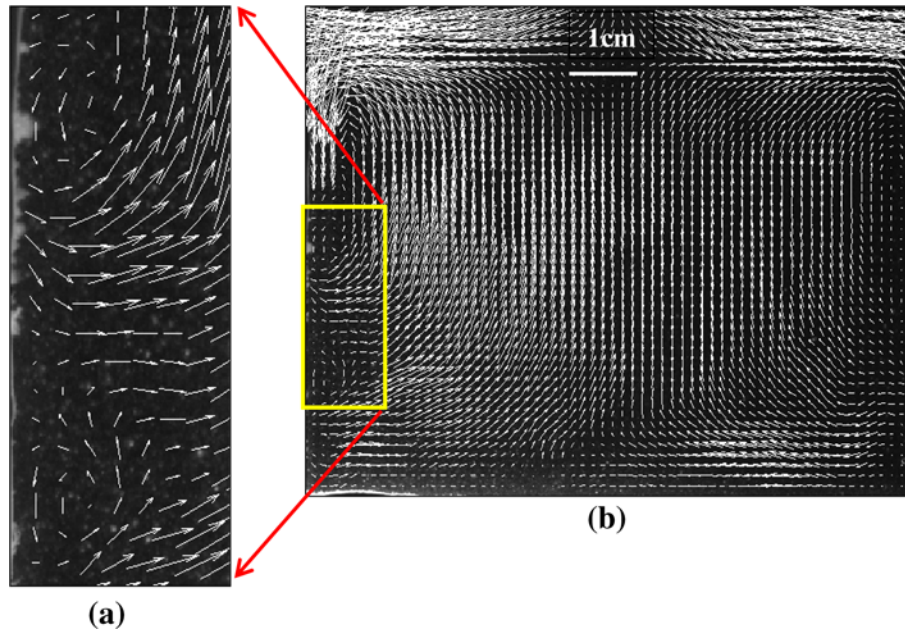
Fig. 6—Measured flow field just after solidification became visible. Due to the formation of dendrites at the walls, eddies were generated close by (*a*) and thus the stable thermal buoyancy stage got more and more disturbed (*b*). Thus, we call this stage of the solidification the perturbed thermal stage (PTH). The measurement was taken $t = 9$ min after switching on the cooling. The velocity vectors were scaled between $v_{min} = 0.169$ mm/s and $v_{max} = 0.57$ mm/s for (a) and between $v_{min} = 0.052$ mm/s and $v_{max} = 0.73$ mm/s for (b). Note that in the zoom (a), some equiaxed crystals are already visible.

the two glass plates. The equiaxed crystallization was very strong (Figure 8(b)), and it represented the leading solidification mechanism. The velocity magnitude was at its maximum. Large crystals appeared even in the bulk far from the vertical walls, and often fell, grouped in columns or in agglomeration. Note that during this stage, most of the solidification process happened. This included the initiation and growth of freckles (flow channels in the mush) where traces can be seen in Figure 9(a). At the end of this stage, the solidification front had almost reached its final position. Stage CC lasted around 10 minutes.

G. *Meandering Flow State (MF): Quasi-Steady Meandering Flow Occurs*

The small eddies disappeared progressively and gave place to a meandering flow traveling from the top to the bottom (Figure 9(a)). The flow is stratified into 5 to 7 circulation layers. It is possible to follow the flow streamlines from the top to the bottom of the cell. The number density of equiaxed crystals decreased in the vicinity of the vertical solidification front and increased in the bulk in the form of a relatively large crystal column or in agglomeration (Figure 9(b)). But, globally equiaxed falls were not as strong as in the previous CC regime. The meander flow seems to penetrate the bottom mushy zone. In this regime, the number of equiaxed crystals and the magnitude of the flow velocity were continuously decreasing in time until extinction. Finally, about 30 pct of the cell volume is filled with solid. Stage MF lasted around 5 to 10 minutes until the typical meandering flow disappeared.

IV. ANALYSIS AND DISCUSSION

The key mechanisms that control the melt flow in the test cell are thermal and solutal convection and drag by columnar and equiaxed crystals. In order to identify the different flow regime that we could encounter, it is useful to compute the global Rayleigh number

$$Ra = \frac{g\beta_T \Delta T \cdot H^3}{\alpha v} + \frac{g\beta_C \Delta C \cdot H^3}{Dv}, \qquad [1]$$

with β_T and β_C being the thermal and solutal expansion coefficients, α the heat conductivity, v the kinematic viscosity, D the diffusion coefficient in the liquid, and g the gravity constant. H is the typical length at which thermal and solutal buoyancy occurs. We have taken the height of the liquid in the test cell as H. ΔT is the temperature difference responsible for thermal buoyancy and ΔC is the concentration difference responsible for solutal buoyancy.

In the present experiment, the highest melt temperature existed at the top middle position in the bulk T_{bulk} and the lowest in the liquid right at the cooled walls, which can be approximated by T_{wall}. We thus took

$$\Delta T = T_{bulk} - T_{wall}. \qquad [2]$$

As for a hypereutectic H_2O-NH_4Cl solution, the solute redistribution coefficient is larger than one ($k > 1$), the formation of NH_4Cl crystals lead to a reduction in melt concentration. Thus, the initial concentration is the highest and the lowest melt concentration occurs right at the cooled walls where solidification has just started. We thus took
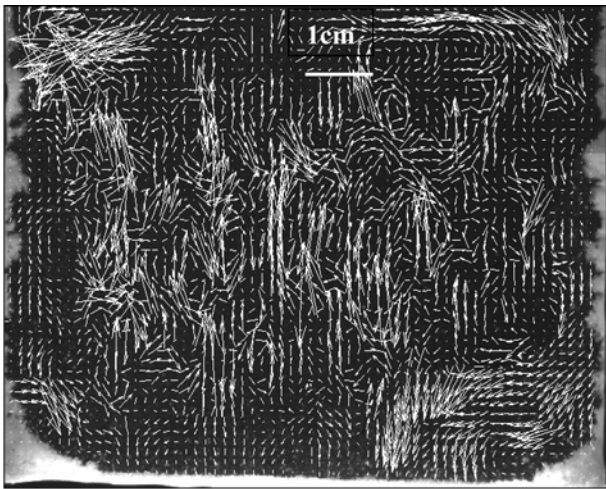
(a)
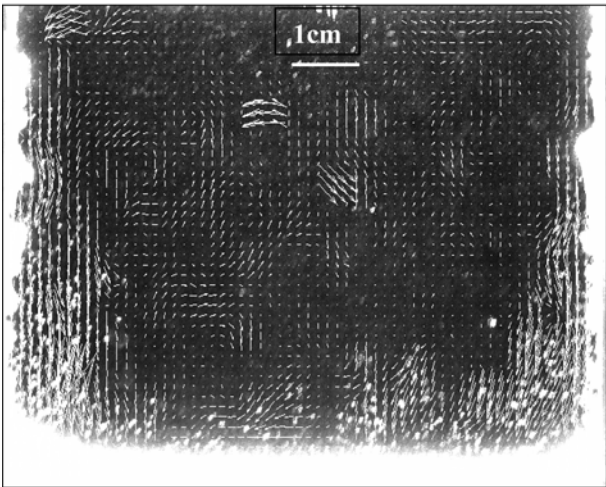
(b)

Fig. 7—When solidification further proceeded, a new flow regime with a large number of small eddies appeared. As described in the text, this regime turned out to be turbulent, and thus we call it the turbulent regime (TU). At this stage, the large number of equiaxed crystals was allowed to measure both the liquid velocity shown in (a) and the velocity of the equiaxed crystals shown in (b). The two-camera PIV measurement was done at $t = 13$ min. The velocity vectors are scaled between $v_{min} = 0.051$ mm/s and $v_{max} = 0.709$ mm/s for the liquid (a) and between $v_{min} = 0.252$ mm/s and $v_{max} = 3.52$ mm/s for the equiaxed crystals (b). Note that the crystals are one order of magnitude faster.

$$\Delta C = C_0 - C(T_{wall}), \quad [3]$$

with $C(T_{wall}) = C_{eutetctic} + m(T_{wall} - T_{eutetctic})$ being the equilibrium concentration at T_{wall} and m the slope of the liquidus temperature being positive for hypereutectic H_2O-NH_4Cl. In the present process, since the temperature and the concentration field are continuously evolving, the magnitude of the global Rayleigh number is consequently changing. To evaluate the Rayleigh number, the main difficulty remains in a good estimation of the magnitude and the time variation of ΔT and ΔC.

In the thermal buoyancy stages (TH1, TH2, TH3), ΔT never exceeds 7 K (7 °C), which is also true during
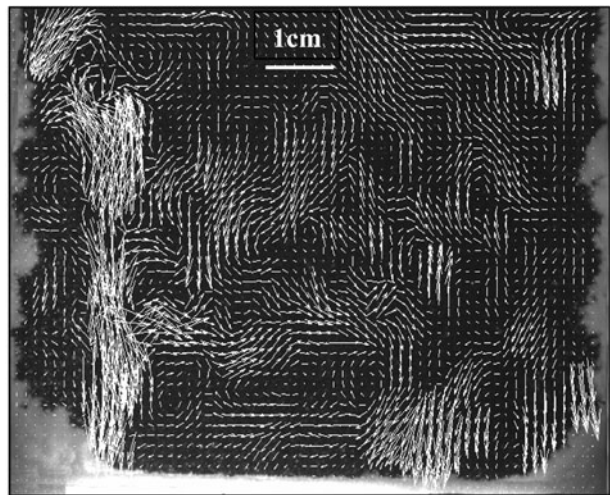
(a)
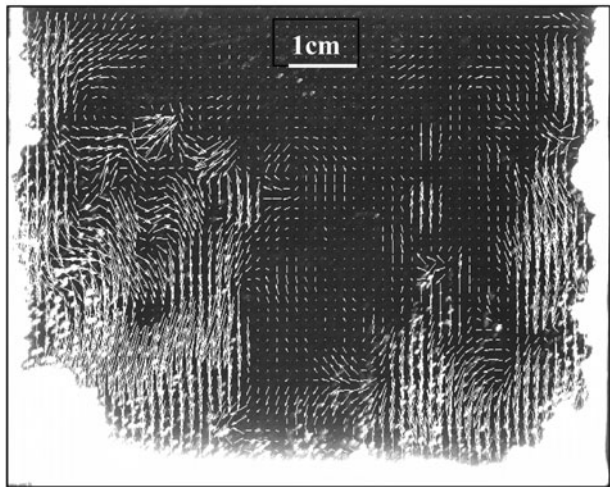
(b)

Fig. 8—Examples showing the melt velocities (a) and the equiaxed crystals' velocities (b) for the so-called coherent CC. The two-camera PIV measurement was done at $t = 15$ min. The velocity vectors are scaled between $v_{min} = 0.111$ mm/s and $v_{max} = 1.56$ mm/s for the liquid (a) and between $v_{min} = 0.278$ mm/s and $v_{max} = 3.87$ mm/s for the equiaxed crystals (b).

solidification. Thus, the thermal Rayleigh number does not exceed 10^8. This is one order of magnitude smaller than the critical number for the occurrence of turbulence. Nevertheless, with the time the wall temperature changes, it is possible to promote unstable behaviors such as those observed at stage TH2. Note that the material properties used to calculate the Rayleigh number are given in Table I.

When the wall temperature reached the liquidus temperature of hypereutectic H_2O-NH_4Cl solution, solidification created ammonium crystals and lower concentrated liquid. This lower concentrated liquid led to a tendency for upward buoyancy and thus contributed to the instabilities observed in the stage PTH. However, the interaction between the flow at the wall and the columnar crystals can also generate eddies. In Figure 6(a), the generation of vortices at the vicinity of few columnar dendrites can be seen. Therefore, it is
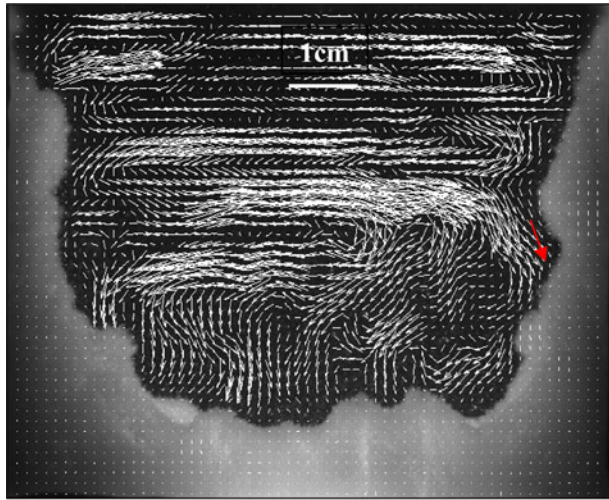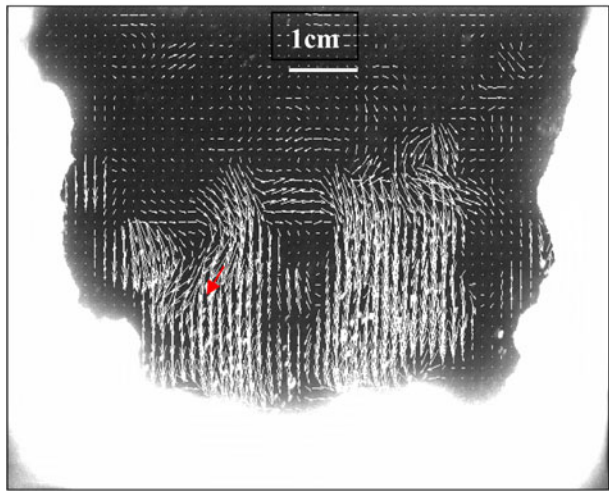
Fig. 9—Examples showing the melt velocities (a) and the equiaxed crystals' velocities (b) for the meandering flow regime (MF). The two-camera PIV measurement was done at $t = 30$ min. The velocity vectors are scaled between $v_{min} = 0.067$ mm/s and $v_{max} = 0.466$ mm/s for the liquid (a) and between $v_{min} = 0.155$ mm/s and $v_{max} = 2.17$ mm/s for the equiaxed crystals (b).

obvious that these perturbations are due to the presence of columnar crystals and not due to the solutal convection. At this stage, the thermal downward jet is strong enough to wash out the low concentration solute rejected during the solidification.

However, with proceeding solidification, solutal convection plays a more important role. Phenomena such as plume dynamics, chaos, or turbulence can appear.[34–36] For a vertical wall, the transition to turbulence occurs at $Ra = 10^9$.[37] With the material properties given in Table I, the solutal Rayleigh number becomes $Ra = 2.2 \times 10^{11} \cdot \Delta C$. Therefore, the critical concentration difference that can lead to the occurrence of turbulence can be estimated to be $\Delta C_{crit} = 0.45$ wt pct which easily occurs during solidification by interdendritic segregation. This means that right from the start of solidification, the flow regime might become turbulent.

Table I. Material Properties of the H_2O-NH_4Cl Solution

Property	Symbol	Value
Density of the liquid	ρ_W	1078 kg/m^3
Density of solid ammonium chloride	ρ_A	1527.4 kg/m^3
Thermal conductivity of the liquid	k_l	0.468 W/m/K
Liquid specific heat	c_{pl}	3249 J/kg/K
Liquid diffusion coefficient	D	4.8×10^{-9} m^2/s
Dynamic viscosity of the liquid	μ	1.3×10^{-3} kg/m/s
Thermal expansion coefficient	β_T	3.832×10^{-4} K^{-1}
Solutal expansion coefficient	β_c	0.257
Eutectic composition	$C_{eutectic}$	19.7 pct NH_4Cl
Eutectic temperature	$T_{eutectic}$	257.75 K

During the first 5 minutes of solidification, the concentration in the bulk can be approximated with the original concentration C_0. At the wall, the rejected solute has a concentration $C (T_{wall})$. At 4 minutes from the start of the solidification (at 13 minutes in Figure 2), the wall temperature reaches 284.15 K (11 °C). Then, $\Delta C \sim 10^{-1}$ and the corresponding Rayleigh number is probably at its maximum and reaches the value of 10^9. This could explain why the measured flow map in stage TU shows such chaotic and incoherent structures, a clear indication of the presence of turbulence. A flow is defined as coherent when the vector field shows clearly its main velocity structure. It must be emphasized that the given Rayleigh number is only an estimated value, it is calculated based on constant physical values found in the literature. Real physical values might be temperature and concentration dependent, which then modify the actual value of the Rayleigh number. But, the order of magnitude found indicates that turbulence in the present solidification process can be generated through solutal buoyancy. Nevertheless, by comparing Figures 7(a) and (b), we can notice that areas where a large number of equiaxed crystals exist are less subject to incoherence. The flow in these regions is well structured in clear streamlines or in large eddies. Obviously, the presence of floating crystals damps the turbulence eddies of the melt flow. Later, with the extension of areas of floating crystals (Figure 8(b)) and the decrease of ΔC, a laminarization of the entire domain occurs.

The evolution in time of the total kinetic energy of the liquid flow calculated with the measured velocity magnitude U as

$$KE = \sum_N \frac{1}{2} U^2 / N \qquad [4]$$

is presented in Figure 10. N is the total number of vectors. In the mushy zone, the velocity vectors are zero. Although there is the presence of some instabilities, no large change in the kinetic energy is observed before the start of solidification. Even if we would have taken the large velocity jets along the walls—which are not completely resolved—into account, the kinetic energy would not change dramatically.

The kinetic energy increased continuously during the perturbed thermal and turbulent regimes. The maximum is reached close to the end of the coherent chaotic regime
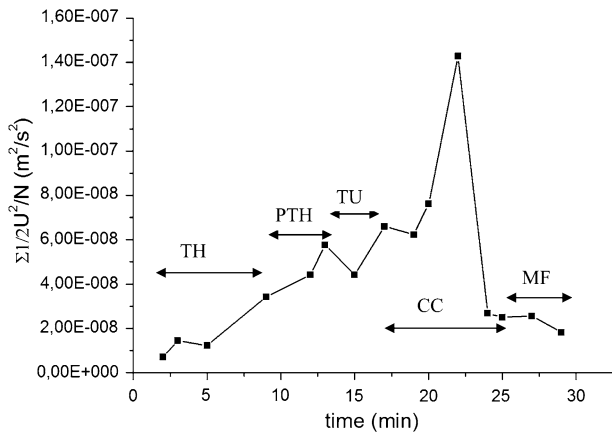
Fig. 10—Evolution of the apparent liquid kinetic energy. The different flow regimes are indicated: TH, thermal stages; PTH, perturbed thermal buoyancy by the start of solidification; TU, turbulent flow; CC, coherent chaotic state; MF, meandering and stratified flow.

(CC) at about $t = 22$ minutes. Later, in the stratified regime (MF), the kinetic energy decreases to levels similar to those of the thermal buoyancy states. This evolution of KE does not correspond to what is reported by Skudarnov et al.,[17] where the velocity decreases in magnitude all along with time. The reason for that might be the fact that in our experiment, we end up in a partly solidified sample where all dynamics fade out with time.

At around 25 minutes, the lower number of equiaxed crystals promotes a steadier and slower melt flow structure (Figure 9(b)). However, the flow path seems to be controlled by the local curves of the dendrite tip envelop. It is probable that the meandering flow regime is created by an auto-organization of the solutal convection in curved constrained geometry (from top to bottom). The concentration differences are small since the evolution of the dendrite tip envelop front is nearly stopped, but large enough to generate a flow KE similar to that of the thermal states.

Since the two vertical glass plates are only 1 cm apart, the flow will have a natural tendency to develop a 2D structure. In PIV analysis found in the literature, the flow was also generally believed to be 2D.[10,16,19–24] If the measurements allow the possibility to follow the flow path, then the flow can be qualitatively considered as two dimensional. Then, the streamlines can be closed, and the life of the eddies can be followed from appearance to dissipation. For our experiment, this was the case for all stages except the turbulent regime where coherence of the flow was totally lost. In the CC, the flow field revealed a clear 2D regime. In addition, the areas around strong chimney jets might also be subject to some turbulence or at least 3D effects.

A. Equiaxed Motion and Interaction with Melt Flow

Another source of energy is the fall of larger equiaxed crystals, which accelerates the melt flow in the vertical direction. A large number of equiaxed crystals can generate large melt flow velocities in some regions. In the present investigation, it was not possible to count the

number of crystals. However, it was possible to estimate the part of the laser sheet that was occupied by large crystals just by looking at the area where the adaptive correlation was successful. At the coherent chaotic state, it became obvious that areas where the melt flow is the most intense correspond to areas where equiaxed crystals occupied large areas of the laser sheet. Thus, it can be concluded that the strong increase of KE between 15 and 23 minutes (Figure 10) is generated by the strong equiaxed crystal motion.

At the end of the experiment, the mushy zone represents 28 pct of the cell volume. According to the phase diagram, only 8 pct of the NH_4Cl mass will solidify. If the entire concentration solidifies in a packed form, it can fill only 6 pct of the cell volume. A simple calculation gives that in average, the mushy zone contains about 25 pct of solid and 75 pct of liquid. However, this is only an average value, the real solid fraction might be much higher at the vicinity of the cold wall and much lower near the solidification front. While the flow enters openly within the bottom mushy zone, it is deviated and curved by the solidification front surface. The vertical mushy regions act almost as nonpermeable media. Perhaps the fact that the vertical mushy regions are built with a succession of equiaxed and columnar layers might explain the difference with the bottom mushy layer. In addition, the sizes of equiaxed crystals that participate in the growth of the vertical walls are smaller than the ones reaching the bottom regions. Using a similarity between packed crystals and packed spheres, the Black-Kozeny law[38–40] predicts that the permeability increases with the crystals' size. These considerations, together with the flow observation, confirm that a strong variation in effective permeability (and porosity) might exist specially all over the surface of the solidification front.

B. Topography of Stationary Mushy Regions

In the presented experiment, solidification is never totally symmetric. This is specially the case at the vertical walls where the topography of the stationary mush possessed an irregular wavy shape. The characteristic size of these waves is 2 to 5 cm in length and 1 to 4 cm in depth (Figure 11). The bottom surface is also subject to variation mainly due to the occurrence of flow chimneys. Irregular columnar growth can be produced by turbulent thermal and solutal fields. The flow vector map suggests that such strong variations exist all along the process. Variation in solutal concentration might produce local remelting of the newly built structure. However, from our experimental observation, it becomes obvious that the main origin of these irregularities is the instability generated from the competition between equiaxed and columnar solidification. For a wavy vertical front, due to the presence of the sedimentation of equiaxed crystals, the wave will develop differently on its upward- and downward-oriented side. This seems to be the case during the regime CC where the sedimentation of equiaxed crystals is particularly strong (Figure 11). Thus, the topography of the mushy zone might develop with a mechanism of crystals
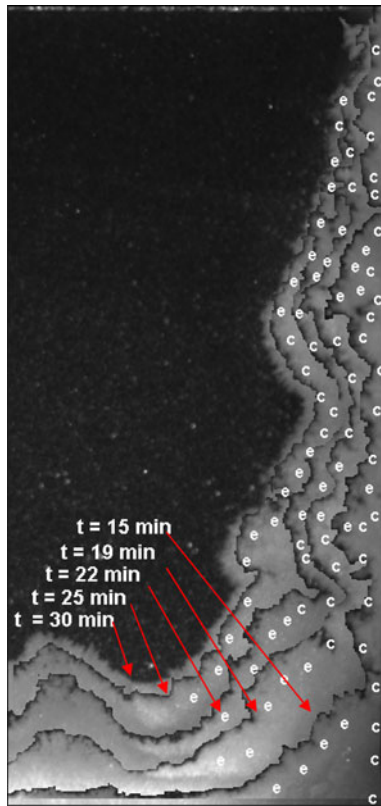
Fig. 11—Nonuniform columnar-equiaxed distribution at the solidification front. (c) indicates a nearly pure columnar dendritic growth front, whereas on the surface (e), equiaxed crystals have sedimented.

clogging on its upward- or vertical-oriented surface, while its downward-oriented surface can only develop through further columnar growth. On the picture, it is possible to observe columnar tips, rarely present on upward-oriented surfaces. In later regimes, as the equiaxed solidification decreases in intensity, the topography of the mushy zone become more and more uniform. At the end of solidification, several layers of equiaxed crystals inclined in the "A" form can be seen.

V. CONCLUSIONS

A special PIV was used to measure the velocity field during a columnar/equiaxed solidification process. The single-phase measurement technique developed for PIV has been extended to cope with liquid-equiaxed flows. It was applied to H_2O-NH_4Cl solidification in a die cast cell of $10 \times 10 \times 1$ cm^3 in which both the liquid velocity and the crystal velocity maps could be extracted. The separation between the two velocity fields could be obtained with the use of fluorescent particles' tracers that emit different waves when excited with the laser wavelength. Two pictures were taken simultaneously with two different cameras; the first one recorded only the laser light through a green filter, while the second one used an orange filter to record only waves emitted by the fluorescent particles. Thus, the first camera could follow only the crystals' paths, while the second camera recorded the liquid velocity field.

During the cooling, different regimes were observed. Before solidification, the flow is controlled by only thermal buoyancy. As soon as the solidification starts, turbulence and chaos are generated in the liquid by a solutal buoyancy mechanism. At the same time, strong equiaxed crystal rains occur at the vicinity of the solidification fronts. At the end of the process, the flow becomes more steady and auto-organizes in a meandering and stratified structure.

A coupling between the fluid flow and the equiaxed crystal was found. In areas with a high crystal density, the turbulence of the flow seems to be damped. The flow in these regions has either large eddies or clear streamlines. However, in the present configuration, it is not yet clear how much is the contribution of the equiaxed rains to the generation of chaos with respect to the solutal buoyancy. Spatio-temporal behavior of the liquid and crystal flow suggested the presence of instabilities and auto-organization often observed in the field of nonlinear systems and chaos. Complex behavior can be expected from the interaction of the flow and equiaxed crystals in larger systems.

REFERENCES

1. FLUENT 6.3: *User's Guide*, Fluent. Inc., Lebanon, NH, 2006.
2. A. Ludwig and M. Wu: *Metall. Mater. Trans. A*, 2002, vol. 33A, pp. 3673–83.
3. R.A. Gore and C.T. Crowe: *J. Fluid Eng. T. ASME*, 1991, vol. 113, pp. 304–07.
4. G. Hetsroni: *Int. J. Multiphase Flow*, 1989, vol. 15, pp. 735–46.
5. D.A. Kalitov and E.K. Longmire: *Exp. Fluids*, 2002, vol. 32, pp. 252–68.
6. A. Kitagawa, Y. Hagiwara, and T. Kouda: *Exp. Fluids*, 2007, vol. 42, pp. 871–80.
7. G. Montante and F. Magelli: *Ind. Eng. Chem. Res.*, 2007, vol. 46, pp. 2885–91.
8. T. Virdung and A. Rasmuson: *Proceedings of the 11th European Conference on Mixing*, VDI-GVC, Bamberg, Germany, 2003, pp. 129–36.
9. C. Beckermann and R. Viskanta: *Appl. Mech. Rev.*, 1993, vol. 46, pp. 1–27.
10. C. Beckermann and C.Y. Wang: *Metall. Mater. Trans. A*, 1996, vol. 27A, pp. 2784–95.
11. C.Y. Wang and C. Beckermann: *Metall. Mater. Trans. A*, 1996, vol. 27A, pp. 2754–64.
12. C.Y. Wang and C. Beckermann: *Metall. Mater. Trans. A*, 1996, vol. 27A, pp. 2765–83.
13. C.L. Lum, M.M. Koochesfahani, and J.J. McGrath: *ASME IM-ECE*, New York, 2001, pp. 1–7.
14. S.Y. Wang, C.X. Lin, and M.A. Ebadian: *Int. J. Heat Mass Transf.*, 1999, vol. 42, pp. 4153–63.
15. S.Y. Wang, C.X. Lin, and M.A. Ebadian: *Int. J. Heat Mass Transf.*, 1999, vol. 42, pp. 4427–45.
16. C. Ghenai, A. Mudunuri, C.X. Lin, and M.A. Ebadian: *Exp. Therm. Fluid Sci.*, 2003, vol. 28, pp. 23–35.
17. P.V. Skudarnov, C.X. Lin, M.H. Wang, N. Pradeep, and M.A. Ebadian: *Int. J. Heat Mass Transf.*, 2002, vol. 45, pp. 5191–5200.

18. Y.-C. Shih and S.-M. Tu: *Appl. Therm. Eng.*, 2009, vol. 29, pp. 2773–82.
19. B. Appolaire, V. Albert, H. Combeau, and G. Lesoult: *ISIJ Int.*, 1999, vol. 39, pp. 263–70.
20. B. Appolaire: Ph.D., INPL, 1999.
21. S. Eck, J. Mogeritsch, and A. Ludwig: *J. Mater. Sci. Forum*, 2006, vol. 508, pp. 157–62.
22. S. Eck, M. Stefan Kharicha, A. Ishmurzin, and A. Ludwig: *Mater. Sci. Eng. A*, 2005, vols. 413–414, pp. 79–84.
23. M. Stefan Kharicha, S. Eck, L. Könöszy, A. Kharicha, and A. Ludwig: *Int. J. Cast Met. Res.*, 2009, vol. 22, pp. 1–4.
24. L. Könözsy, M. Stefan Kharicha, S. Eck, M. Wu, and A. Ludwig: *Mater. Sci. Forum*, 2010, vol. 649, pp. 367–72.
25. R.J. Adrian: *Annu. Rev. Fluid Mech.*, 1991, vol. 23, pp. 261–304.
26. Z.-C. Liu, C.C. Landreth, R.J. Adrian, and T.J. Hanratty: *Exp. Fluids*, 1991, vol. 10, pp. 301–12.
27. C. Willert, B. Stasicki, M. Raffel, and J. Kompenhans: *SPIE Proc.*, 1995, vols. 2546–2519, pp. 32–39.
28. K. Okamoto and M. Oki: *International Conference on Advanced Optical Diagnostics in Fluids, Solids and Combustion*, Tokyo, Japan, 2004, pp. 1–5.
29. Y.A. Hassan: *Ann. N. Y. Acad. Sci.*, 2002, vol. 972, pp. 223–28.
30. J. Westerweel: *Meas.-Sci. Technol.*, 1997, vol. 8, pp. 1379–92.
31. J. Westerweel: Ph.D., Technical University of Delft, 1993.
32. S. Kumar and S. Banerjee: *Phys. Fluids*, 1998, vol. 10, pp. 160–77.
33. J. Nogueira, A. Lecuona, and P.A. Rodriguez: *Meas. Sci. Technol.*, 1997, vol. 8, pp. 1493–501.
34. C. Beckermann, C. Fan, and J. Mihailovic: *Int. Video J. Eng. Res.*, 1991, vol. 1, pp. 71–82.
35. C. Bizon, J. Werne, A.A. Predtechensky, K. Julien, W.D. McCormick, J.B. Swift, and H.L. Swinney: *Chaos*, 1997, vol. 7, pp. 107–24.
36. S. Schoofs and F.J. Spera: *Transp. Porous Med.*, 2003, vol. 50, pp. 179–95.
37. A. Bejan: *Heat Transfer*, Wiley, New York, 1993.
38. N. Zabaras and D. Samanta: *Int. J. Numer. Methods Eng.*, 2004, vol. 60, pp. 1103–38.
39. C.Y. Wang, S. Ahula, C. Beckermann, and H.C. de Groh, III: *Metall. Mater. Trans. B*, 1995, vol. 26B, pp. 111–19.
40. A. Badillo, D. Ceynar, and C. Beckermann: *J. Cryst. Growth*, 2007, vol. 309, pp. 197–215.